AGU PUBLICATIONS

Geophysical Research Letters

RESEARCH LETTER
10.1002/2017GL075424

**Key Points:**
- Diopside transforms to $\gamma$-diopside with penta-coordinated silicon through high pressure and ambient temperature
- Penta-coordinated silicates can be possible intermediate phases between four- and six-coordinated silicates
- Metastable pyroxene and postpyroxene phases are important for explaining slab stagnation, seismic anisotropy, and deep-focus earthquakes

**Supporting Information:**
- Supporting Information S1
- Data Set S1
- Data Set S2
- Data Set S3
- Data Set S4

**Correspondence to:**
P. Dera,
pdera@hawaii.edu

**Citation:**
Hu, Y., Kiefer, B., Bina, C. R., Zhang, D., & Dera, P. K. (2017). High-pressure $\gamma$-$CaMgSi_2O_6$: Does penta-coordinated silicon exist in the Earth's mantle? *Geophysical Research Letters*, *44*, 11,340–11,348. https://doi.org/10.1002/2017GL075424

Received 25 AUG 2017
Accepted 22 OCT 2017
Accepted article online 26 OCT 2017
Published online 18 NOV 2017



# High-Pressure $\gamma$-$CaMgSi_2O_6$: Does Penta-Coordinated Silicon Exist in the Earth's Mantle?

**Yi Hu[1,2], Boris Kiefer[3], Craig R. Bina[4], Dongzhou Zhang[2], and Przemeslaw K. Dera[1,2]**

[1]Department of Geology and Geophysics, School of Ocean and Earth Science and Technology, University of Hawaii at Manoa, Honolulu, HI, USA, [2]Hawaii Institute of Geophysics and Planetology, School of Ocean and Earth Science and Technology, University of Hawaii at Manoa, Honolulu, HI, USA, [3]Department of Physics, New Mexico State University, Las Cruces, NM, USA, [4]Department of Earth and Planetary Sciences, Northwestern University, IL Evanston, USA

**Abstract** In situ X-ray diffraction experiments with natural Fe- and Al- bearing diopside single crystals and density functional theory (DFT) calculations on diopside end-member composition indicate the existence of a new high-pressure $\gamma$-diopside polymorph with rare penta-coordinated silicon. On compression $\alpha$-diopside transforms to the $\gamma$-phase at ~50 GPa, which in turn, on decompression is observed to convert to the known $\beta$-phase below 47 GPa. The new $\gamma$-diopside polymorph constitutes another recent example of penta-coordinated silicon ($^{V}$Si) in overcompressed metastable crystalline silicates, suggesting that $^{V}$Si may exist in the transition zone and the uppermost lower mantle in appreciable quantities, not only in silicate glass and melts but also in crystalline phases contained in the coldest parts of subducted stagnant slabs. $^{V}$Si may have significant influences on buoyancy, wave velocity anomalies, deformation mechanisms, chemical reactivity of silicate rocks, and seismicity within the slab.

**Plain Language Summary** Earth is a rocky planet and is dominated by silicates. Crust and upper mantle of our planet feature minerals with silicon almost exclusively in four-coordinated sites, whereas minerals with silicon in six-coordinated sites dominate the transition zone and the lower mantle. It is a long-standing question whether five-coordinated Si phases exist. Five-coordinated Si is observed in silicate glass and melt upon compression as intermediate states and can provide important insight into the transformation mechanism in silica densification. In this paper, we observed a high-pressure crystalline silicate phase with five-coordinated Si. This affects chemical reactivity, elastic and plastic deformation, density of the subducted slab, and its buoyancy relative to the surrounding mantle.

## 1. Introduction

The Earth's mantle is primarily composed of silicates. The pressure-induced transformations of the silicate minerals strongly affect the physical properties of the Earth's mantle and therefore controls geological processes such as tectonics and deep-focus earthquakes. Si strongly prefers four-coordinated crystallographic sites due to $sp^3$ hybridization. As a consequence, in silicate minerals characteristic of the crust and the upper mantle, silicon resides predominantly in tetrahedral sites coordinated by four oxygen atoms ($^{IV}$Si). This low coordination number and mesodesmic bonds, found, for example, in quartz, pyroxene, and olivine, result in significant structural flexibility for forming extended silicate chains, sheets, and framework polyhedral motifs and accounts for the majority of the mineral diversity observed in terrestrial rocks of shallow origin. Silicon is also capable of forming hypervalent, five- and six- coordinated states ($^{V}$Si and $^{VI}$Si). These hypervalent states are favored at high pressures and with increased ligand electronegativity. As a result, at greater depths of the Earth's interior, silicon strongly prefers sites with six nearest neighbor ligands arranged in octahedral geometry, leading to more compact, higher-density phases such as $SiO_2$ stishovite, $(Mg,Fe)SiO_3$ bridgmanite or $MgSiO_3$ akimotoite. Densification of silicates, involving a coordination number increase from four ($^{IV}$Si) to six ($^{VI}$Si) accounts for the density stratification of the Earth's mantle and is responsible for the 660 km seismic discontinuity.

There has been great interest in understanding the occurrence and function of the penta-coordinated Si phases ($^{V}$Si) both in solid state chemistry and Earth science. Stereochemical analysis of crystal structures reported to contain $[SiL_5]$ groups (where L represents ligand such as C, N, F, or Cl) in crystals with hexagonal close-packed arrays of ligands indicates that there is an almost continuous change from an $[SiL_4]$ tetrahedron

to an [$SiL_5$] trigonal bipyramid and that the penta-coordinated state indeed plays a critical role as intermediate in condensation and decondensation reactions of silicates in aqueous solutions and in melts (Liebau, 1984). Amorphous solids and melts can sustain exotic coordination environments such as $SiO_5$ more easily than crystalline silicates due to the lack of symmetry and long-range order. Indeed, several studies of glass and melts clearly indicate existence of penta-coordinated silicon at elevated pressures, which can sometimes persist in quenched samples. It is also believed that penta-coordinated silicon plays an important role in dissolution of silica and change of deformation mechanism (Yuan & Huang, 2014). Crystalline silicate minerals with $^{V}$Si are rare, but have been reported previously in the literature based on both experiments and calculations and are suggested as important intermediate phases in phase transformation and chemical reaction processes. For example, a quenchable phase with five-coordinated Si was observed in $CaSi_2O_5$ silicate, which can be synthesized at 1,500°C and 10 GPa (Angel et al., 1996). A nonquenchable high-pressure polymorph of enstatite (Finkelstein et al., 2015) and a high-pressure phase of danburite (Pakhomova, Bykova, et al., 2017) observed in single crystal X-ray diffraction experiments also featured $^{V}$Si. Molecular dynamics calculations predicted that $^{V}$Si coordination should form in $SiO_2$ $\alpha$-quartz under uniaxial stress at high pressure (Badro et al., 1997). High-pressure states involving $^{V}$Si are also reported to act as intermediates during the $^{IV}$Si to $^{VI}$Si transition in molecular dynamics simulations on $\alpha$-quartz (Hu, Shu, et al., 2015) and orthoenstatite (Chaplot & Choudhury, 2001). Pyroxenes are the second most abundant mineral group in the Earth's upper mantle and represent a major mineral component in subducted slabs, which are composed of upper mantle rocks (residual harzburgite and lherzolite), containing up to 30% pyroxene (Ita & Stixrude, 1992), and basaltic crust layer, where the pyroxene content may be as high as 70% (Ringwood, 1982). Diopside ($CaMgSi_2O_6$), the Mg,Ca-end-member clinopyroxene (cpx), is abundant in both the upper mantle and the subducted lithosphere (Ringwood, 1982). At ambient conditions, diopside crystallizes in C2/c space group and is thermodynamically stable up to ~18 GPa. Above this pressure and 1,400°C diopside decomposes into a mixture of product phases including $CaSiO_3$-rich perovskite and Mg-rich $(Mg,Ca)SiO_3$ tetragonal garnet. Below 1,400°C, diopside dissociates to Ca-perovskite + wadsleyite + stishovite (Akaogi et al., 2004; Canil, 1994; Kim et al., 1994; Oguri et al., 1997). At pressures above 20 GPa, between 1,000°C and 1,900°C, diopside is observed to break down to Mg-perovskite and Ca-perovskite (Irifune et al., 2000; Liu, 1979). Subsequently, a metastable cubic CM-perovskite $Ca(Mg,Fe,Al)Si_2O_6$ phase was observed to form at ~1,300°C and 32 GPa and was also observed in diopside glass at ~1,000°C and 13 GPa as a metastable phase. At 1,800°C, CM-perovskite was observed to decompose into cubic Ca-perovskite and orthorhombic Mg-perovskite and stishovite (Asahara et al., 2005; Kim et al., 1994).

In the more chemically and petrologically complex upper mantle and transition zone, where temperature is high (>1,400°C), pyroxene is believed to gradually dissolve into garnet and form majorite around depths corresponding to the transition zone (Ita & Stixrude, 1992). However, the mantle transition zone is not homogeneous in temperature and chemical composition. Seismic tomography observations show that some cold subducted slabs in the west Pacific regions stagnate at the bottom of transition zone or the uppermost lower mantle (Fukao & Obayashi, 2013; Fukao et al., 2009). Geodynamic models estimate the temperature in the stagnant slabs are lower than 900°C and can be as low as 500°C in regions such as Tonga (Ganguly et al., 2009; King et al., 2015). It has been reported that, in cold environment (<1,400°C), the diffusion between pyrope and majorite garnet is slow, making the preservation of the light metastable pyroxene possible, which changes the density of the slab and therefore affects its morphology and buoyancy (Agrusta et al., 2014; Faccenda & Dal Zilio, 2017; King et al., 2015; Nishi et al., 2008, 2009, 2011, 2013; Van Mierlo et al., 2013). As a consequence, the metastability of pyroxene and the kinetics of postpyroxene transformations below 1,000°C have been suggested to play an important role in slab dynamics (Faccenda & Dal Zilio, 2017; Nishi et al., 2011; Van Mierlo et al., 2013).

High-pressure ambient-temperature experiments not only pave the road to high-pressure moderate-temperature ($500°C < T < 1,000°C$) experiments but also create conditions to trap the metastable intermediate phases which can provide important transition path information for future kinetic studies. On compression at ambient temperature, diopside can be metastably preserved to pressures as high as 50 GPa (Chopelas & Serghiou, 2002; Thompson & Downs, 2008), above which it transforms to $\beta$-phase with mixed four- and six-coordinated silicon (Plonka et al., 2012). A similar structure was also observed in clinoferrosillite $FeSiO_3$ at high pressure (Pakhomova, Ismailova, et al., 2017). Other clinopyroxenes were also observed to be preserved to at least 30 GPa at ambient temperature (Hu, Dera, et al., 2015; Xu et al., 2017; Zhang et al., 2016). Natural diopside typically contains appreciable amounts of iron, and the objective of this study is to examine

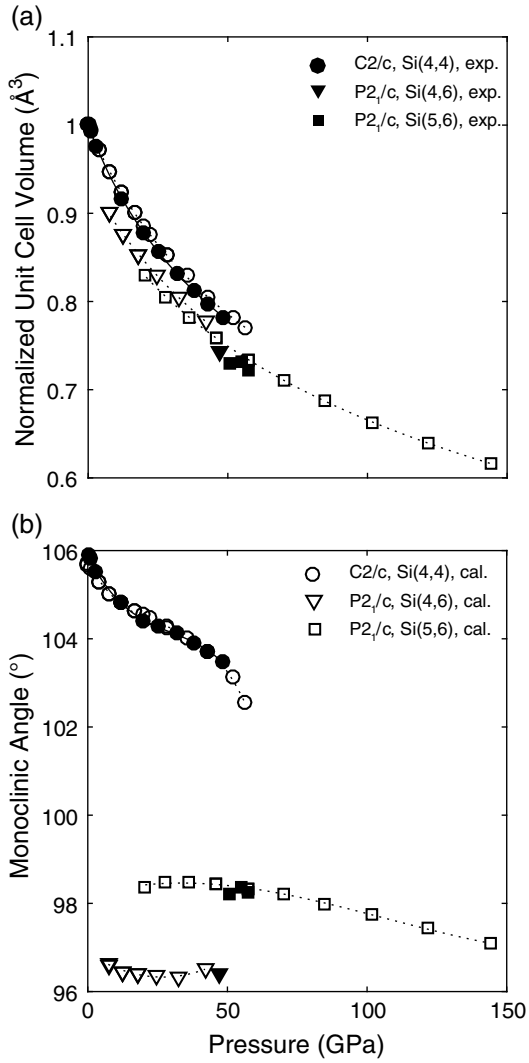


**Figure 1.** (a) Normalized unit cell volume of different diopside phases with respect to $V_0$ of $\alpha$-diopside. Solid line is the third-order Birch-Murnagham equation of state fit of the XRD experimental data, and dotted lines are the third-order Birch-Murnagham equation of state fit of the DFT calculation results. (b) Monoclinic angles of different diopside phases. C2/c Si(4, 4) $\alpha$-diopside (circles), $P2_1/c$ Si(4, 6) $\beta$-diopside (down pointing triangles) and $P2_1/c$ Si(5, 6) $\gamma$-diopside phases (squares) at high pressure. Filled symbols are from XRD experiments on Fe- and Al-bearing diopside (errors are smaller than the markers) and open symbols are from DFT calculations on $Di_{100}$.

the effect of iron on the postpyroxene transformation in natural samples along the diopside-hedenbergite join. In this study, we combined in situ single crystal synchrotron X-ray diffraction experiments on a natural iron-bearing diopside sample with density-functional-theory (DFT) calculations, to better understand the formation of exotic hypervalent silicon states in pyroxenes.

## 2. Methods

The sample used for synchrotron experiments was a natural Fe- and Al-bearing diopside with composition $(Ca_{1.86}Fe^{2+}_{0.10}Na_{0.03}Mn_{0.01})(Mg_{0.75}Fe^{2+}_{0.15}Al_{0.07}Fe^{3+}_{0.02}Ti_{0.01})(Si_{1.94}Al_{0.06})O_6$ from the Harry Hess collection at Princeton University. Single crystal X-ray diffraction (SXD) experiments were conducted at the University of Hawaii and at the synchrotron beamline 13-ID-D of the Advanced Photon Source at Argonne National Laboratory. Data was analyzed by GSE_ADA/RSV (Dera et al., 2013) and SHELXL package (Sheldrick, 2008). Three-dimensional periodic density functional theory (DFT) calculations were performed using VASP (Vienna Ab initio Simulation Package) (Kresse & Furthmüller, 1996a; 1996b). The experimental and calculation details are described in supporting information Text S1 (Angel et al., 1996; Badro et al., 1997; Blöchl, 1994; Dera et al., 2013; Finkelstein et al., 2015; Holzwarth et al., 1997; Horiuchi, 1987; Hu, Dera, et al., 2015; Kresse & Furthmüller, 1996a, 1996b; Mao et al., 1986; Momma & Izumi, 2011; Morimoto, 1988; Perdew & Zunger, 1981; Sheldrick, 2008; Subramanian, 1962; Walker, 2012; Walker et al., 2008).

## 3. Results and Discussion

At ambient conditions, in the $\alpha$-phase, diopside has a C2/c space group and retains this symmetry to at least 48.4(1) GPa, when compressed at ambient temperature (Table S1). The $\alpha$-phase is characterized by a monoclinic angle of ~105° and all Si in tetrahedral coordination. Upon further compression, the Fe- and Al-bearing diopside undergoes a phase change to a $P2_1/c$ $\gamma$-phase with a decrease in volume and a change in monoclinic angle to ~98° at ~55.1(1) GPa (Figure 1 and Table S1). Our refinements reveal a structure with a mixture of $^{V}$Si and $^{VI}$Si polyhedral layers. Unlike the case of experiments with end-member diopside, which transformed from $\alpha$ to $\beta$-phase, converting a single tetrahedral $^{IV}$Si site into a 1:1 mixture of $^{IV}$Si and $^{VI}$Si (Plonka et al., 2012), compression of the natural diopside sample results in a change to the coordination number of both Si sites in the $P2_1/c$ structure, producing hypervalent five- and six-coordinated polyhedra. Whereas this discrepancy could be attributed to the different chemical composition, it is also possible that the previous experiments simply did not reach high enough pressure to reveal the $\gamma$-phase in the end-member. Upon decreasing pressure, the $\gamma$-phase is preserved to ~51 GPa. At ~47 GPa, $\gamma$-diopside undergoes an isosymmetric phase transition to the $P2_1/c$ $\beta$-phase with monoclinic angle changing to ~96° (Table S1). The transition pressure from C2/c phase to $P2_1/c$ phase is very close to what was observed in previous shock experiments, which reported a thermomechanical phase transformation at ~50 GPa (Svendsen & Ahrens, 1983). Our experiments were complemented by a series of first-principles computations, to explore the origin of the exotic $^{V}$Si coordination further. The unit cell parameters of the three phases obtained from both experiments and calculations are shown in Figures 1 and S2. The enthalpy calculated by density functional theory indicates that the $P2_1/c$ structure becomes energetically favorable over C2/c structure from ~30 GPa and the five- and six-coordinated $P2_1/c$ transition takes place above ~38 GPa, which corresponds to the pressure of the uppermost lower mantle (Figure S3). Once locked in the five-coordinated configuration, diopside can remain in this structure without transforming to six-coordinated structure to ~150 GPa. The discrepancy between

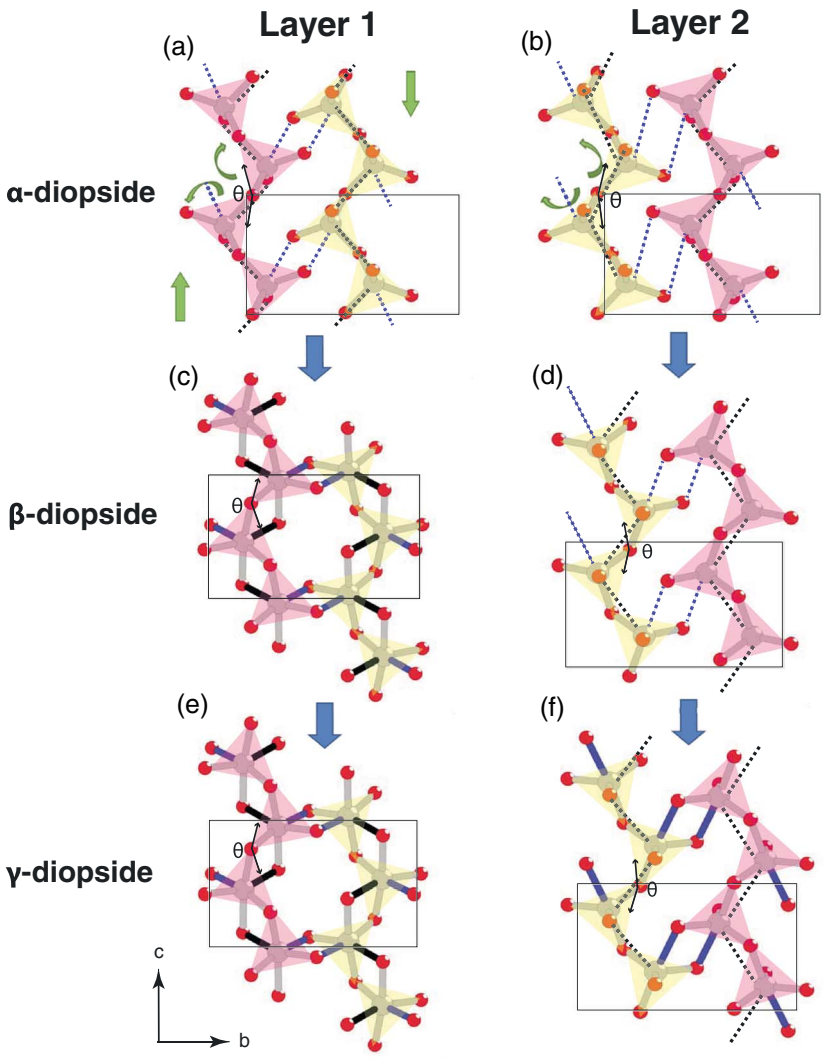


**Figure 2.** (a) Layer 1 of C2/c $\alpha$-diopside phase with $^{IV}Si^{4+}$. $\theta$ is the O3-O3-O3 angle. Green arrows show the Si-O chain rotation and translation. (b) Layer 2 of C2/c $\alpha$-diopside phase with $^{IV}Si^{4+}$. $\theta$ is the O3-O3-O3 angle. (c) Layer 1 of $P2_1/c$ $\beta$-diopside phase with $^{VI}Si^{4+}$. $\theta$ is the O3a-O3a-O3a angle. (d) Layer 2 of $P2_1/c$ $\beta$-diopside phase with $^{IV}Si^{4+}$. $\theta$ is the O3b-O3b-O3b angle. (e) Layer 1 of $P2_1/c$ $\gamma$-diopside phase with $^{VI}Si^{4+}$. $\theta$ is the O3a-O3a-O3a angle. (f) Layer 2 of $P2_1/c$ $\gamma$-diopside phase with $^{V}Si^{4+}$. $\theta$ is the O3b-O3b-O3b angle. Si and O atoms are represented by grey and red, respectively. Solid black rectangular box is the unit cell. Same color denotes the same Si-O distance in different figures. Magenta solid triangle facets represent O-O-O planes above Si atoms and green solid triangles facets represent O-O-O planes above Si atoms. Si-O distances and polyhedral parameters are listed in Table S5.

experimentally observed and computationally determined transition pressures can be attributed to kinetic effects, as well as absence of thermal contributions in the computations. In the DFT calculations we also found two other structural variants—one with $^{IV,VI}Si^{4+}$ in $P2_1/c$ space group and one with $^{V,V}Si^{4+}$ in C2/c space group, which do not manifest themselves in nature.

Based on experimental observations, we propose a model explaining how $\alpha$-diopside transforms to the $\beta$ and $\gamma$-phases. C2/c $\alpha$-diopside is described by corner-sharing $SiO_4$ tetrahedral chains that extend along the *c* axis. Between these Si-O chains, $Ca^{2+}$ and $Mg^{2+}/Fe^{2+}$ cations are placed for charge neutrality. The I beam representation of building blocks of the pyroxene structure conveniently shows that each octahedral layer is intimately connected to two silicate chain layers on either side by sharing oxygen atoms (Figure S4a). In the C2/c $\alpha$-diopside phase, there is only one unique Si site (Table S2). The Si atoms in different layers are related by a (1/2, 1/2, 0) translation symmetry (C centering). After the C2/c to $P2_1/c$ phase transformation, the C centering is lost, producing two symmetry-independent Si-O layers (Tables S3 and S4). As a consequence, there are two

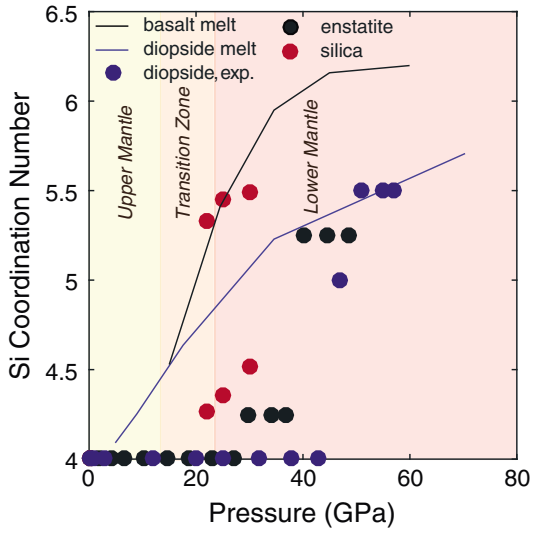


**Figure 3.** Si coordination number of basalt melt (black line) (Sanloup et al., 2013), diopside melt (blue line) (Sun et al., 2011), enstatite (black circle) (Finkelstein et al., 2015), silica (magenta circle) (Badro et al., 1997), and diopside (this study) (blue circle). The different colors of background indicate the upper mantle (yellow), the transition zone (orange), and the lower mantle (red) regions.

unique sites for Si cations (Si1 and Si2) in the $P2_1/c$ phase, residing in two different layers. We denote Si-O layer with Si1 as layer 1, while the layer containing Si2 is denoted as layer 2 (Figure S4b). The same transformation also applies to the O anions—the three different O sites in C2/c phase split into six unique O sites in the $P2_1/c$ phase. In the $P2_1/c$ structure the oxygen atoms occupy general positions and therefore possess a degree of translational freedom to respond to changes in applied pressure, which is absent in C2/c symmetry.

At low temperatures, the kinetic energy available for atomic rearrangements accompanying structural transitions is limited, and as a result, displacive phase transformations are favored. As pressure increases, the Si-O layers become more condensed and the Si-O chains start to interconnect, as shown in Figure 2. In layer 1, the conversion involves two steps: a shift of the Si-O chains and rotation of the Si-O tetrahedra, which result in the formation of six-coordinated silicon (Figure 2). Si#0-O2#2 and Si#0-O1#1 distance in C2/c phase are denoted by blue and black dashed lines in Figure 2a and markers with the same color in Figure S5. Both distances decrease gradually as pressure increases and new bonds form after the phase transformation. In the $P2_1/c$ phases, Si#0 becomes Sia#1, while O2#2 and O1#0 become O2a#0 and O1a#0, respectively. Sia#1 connects with O2a#0 (the blue bond) and O1a#0 (the black bond), forming edge-sharing Si-O octahedral layers with $^{VI}$Si (Figures 2c and 2e). These new bonds cause the oxygen layers to shift, and the O-O-O ($\theta$) angle change from ~150° to 200° (Table S5) ($\theta$ is labeled in Figure 2). As can be seen from Figures 2c and 2e, one chain of O atoms shifts by approximately c/2, along the *c* axis and the $SiO_4$ polyhedra rotate by ~50° ($\theta$ angle). In layer 2, Si#3-O2#5 and Si#3-O1#6 in C2/c phase are denoted by blue and black dashed lines in Figure 2b. Both distances first decrease and then increase as pressure increases within C2/c phase. This behavior makes it difficult for Si and O to approach close enough to form a bond. After the C2/c-$P2_1/c$ phase transformation, Si#3 turns into Sib#3, while O2#5 and O1#6 turn into O2b#5 and O1b#6. Both distances decrease dramatically, but only Sib#3-O1b#5 becomes a bond (Figures S5b, 2d, and 2f). The fifth Si-O interatomic distance in $\gamma$-diopside phase has a length of ~1.9 Å. At 55.1(1) GPa, electron density map is calculated by DFT and a bond path can be seen (Figure S6), confirming the attractive character of this interatomic interaction. A similar structure with 4 + 1-coordinated Si is also observed in postenstatite (Finkelstein et al., 2015). The fact that pyroxenes go through penta-coordinated structures suggests such structure could be a common intermediate between the four- to six-coordinated transformations in pyroxenes. The bond-forming characteristics of the phase transformation between $\alpha$ and $\gamma$-diopside suggest exothermic reaction, which is one of the criteria for phase transformations that could be responsible for deep-focus earthquakes (Hogrefe et al., 1994).

The dominant coordination state of Si in the Earth's upper mantle and transition zone is $^{IV}$Si, whereas in the lower mantle it changes to $^{VI}$Si (Frost, 2008). This change in coordination number and geometry of $SiO_N$ ($N = 4$, 5, 6) units is determined by different electron orbital hybridization types. The tetrahedral geometry of $SiO_4$ group (Figure S7a) is caused by $sp^3$ hybridization of the Si orbitals, while the octahedral geometry of $SiO_6$ group (Figure S7c) is a result of $sp^3d^2$ hybridization (Tandura et al., 1986). Most of the penta-coordinated silicate structures reported to date have approximately square pyramid configuration with bond lengths ranging from ~1.6 to ~1.9 Å, averaging ~1.7 Å, as shown in Figures S7d–S7f (Angel et al., 1996; Badro et al., 1997; Finkelstein et al., 2015). Geometrically, these structures suggest the $sp^3d^2$ hybridization with a lone electron pair. However, the $SiO_5$ group in this study shows a trigonal bipyramid structure with four bond lengths ranging from 1.60(2) to 1.67(2) Å and the fifth bond length of 1.95(2) Å which suggests a $sp^3d$ hybridization (Figure S7b) (Tandura et al., 1986). Theoretical studies also suggest that hypervalent Si compounds feature three-center-four-electron (3c-4e) electron-deficient bond. This predicts elongated Si-O bond length along the axial direction, as observed in the current study. Previous reports demonstrate that the Si-O bond could be as long as 1.954 Å and 1.918 Å in organic compounds due to the weak bonding character of the 3c-4e bonds (Holmes, 1996). Hypervalent compounds exhibit high Lewis acidity because the electron density on the central atom decreases with increasing coordination. For example, methanium ($CH^{5+}$), which can be explained

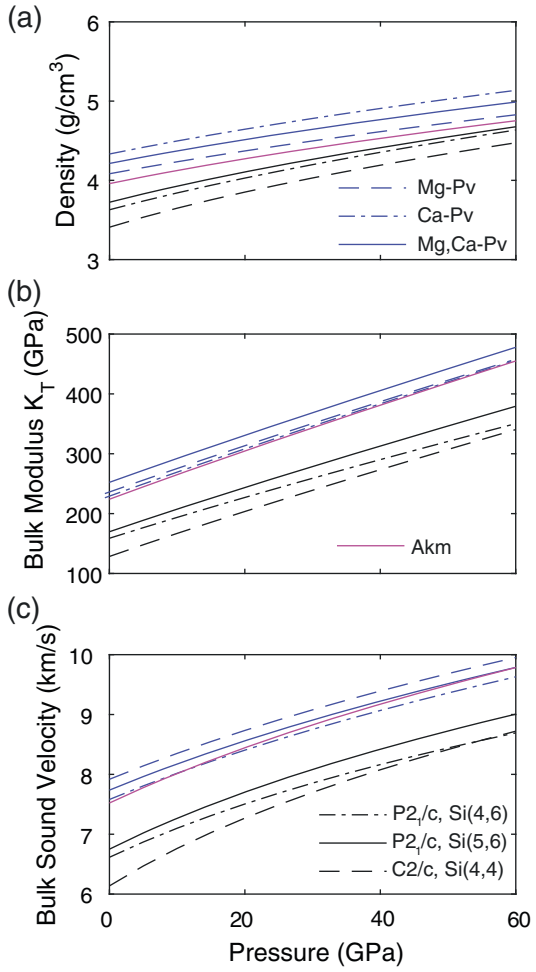


**Figure 4.** (a) Density, (b) bulk modulus, and (c) bulk sound velocities of different mineral phases calculated by DFT. Mg-perovskite data are from Wentzcovitch et al. (2004). Ca-perovskite data are from Caracas et al. (2005). Mg, Ca perovskite data are from simple linear interpolation of Mg perovskite and Ca perovskite. Mg ilmenite data are from Karki et al. (2000). $P2_1/c$ Si(4,6), $P2_1/c$ Si(5,6), and C2/c Si(4,4) are from our DFT calculation results.

by the electron-deficient 3c-2e chemical bond, is a superacid (Rasul et al., 2011; White et al., 1999). The occurrence of $^{V}$Si in chemical compounds has been reported to result in greatly increased chemical activity (Holmes, 1996); therefore, the presence of $^{V}$Si in $\gamma$-diopside and other metastable hypervalent mantle silicate phases could be expected to alter chemical reactions taking place during melting and mantle convection.

The coordination number of Si in both amorphous/liquid and crystalline silica/silicates increases with increasing pressure (Figure 3). In basalt and diopside melt, this increase is continuous and the $^{IV}$Si - $^{VI}$Si jump takes place between 20 and 50 GPa, which roughly corresponds to the transition zone and top of the lower mantle (Frost, 2008). Si coordination changes in enstatite (Finkelstein et al., 2015) and silica (Badro et al., 1997) indicate very similar behavior, with densification starting at lower mantle pressures. In this study, the average coordination number of crystalline diopside reaches 5 (4 + 6) in the $\beta$-phase around 40 GPa, and increases to 5.5 (5 + 6) in the $\gamma$-phase around 50 GPa; however, this pressure is likely to decrease at elevated temperature. The Si coordination number in melts and glasses is known to affect the rheological behavior because of the formation and breakdown of bonds (Yuan & Huang, 2014). It can also be expected to affect the properties of crystalline material in similar ways. Diopside is brittle and exhibits good natural cleavage on {110}, with intersects at 87° and 93° due to the weak bonding between Si-O tetrahedral chains, as shown in Figure S4a. Both the $\beta$ and $\gamma$ hypervalent-Si diopside phases show structures in between pyroxene and ilmenite, and the fact that the Si-O tetrahedral chains become connected will make it harder to fracture the crystals in the pyroxene manner, because ilmenite structure does not have natural cleavage. Slip systems, which control the lattice-preferred orientation of clinopyroxenes have been reported to be {110}1/2, {110}[001] and (100)[001] (Zhang et al., 2006). The new bonds in $P2_1/c$ phases which form in {110} planes will most likely reduce the mobility on the original {110} planes and therefore may change lattice preferred orientation. The presence of $SiO_5$ defects was also recently suggested to play a critical role in the brittle to ductile transition in densified silica glass by facilitating shear deformation and in dissipating energy by converting back to the fourfold coordination state during deformation (Yuan & Huang, 2014). If $^{V}$Si is also present in crystalline silicates, the condensed silicate layers may have a similar effect on the rheology of the mantle rocks.

Slabs have been detected to be stagnant at the mantle transition zone depth, especially in cold and old subducted slabs in the west Pacific regions where the estimated temperatures at 660 km are below 1,000°C (Fukao & Obayashi, 2013; Fukao et al., 2009; King et al., 2015). The preservation of light metastable phases such as olivine to compensate the effect of low temperature thus providing buoyancy force is one of the proposed mechanisms (Bina & Kawakatsu, 2010; Kirby et al., 1996; Marton et al., 1999; Rubie & Ross, 1994; Schmeling et al., 1999; Tetzlaff & Schmeling, 2000). It has been suggested that the pyroxene-garnet transformation can be kinetically sluggish in cold environments, and thus pyroxene may be preserved in subduction zones at least to the top of the lower mantle (Nishi et al., 2013; Van Mierlo et al., 2013). Recent geodynamic modeling has demonstrated that metastable pyroxene has a stronger potential for affecting slab buoyancy at the transition zone than metastable olivine, though has not yet accounted for the post-pyroxene transformation involving Si coordination changes (Agrusta et al., 2014; King et al., 2015).

The preservation of pyroxene and post-pyroxene phases changes the density and elastic properties of the slab, and therefore affects morphology and seismic wave velocity profile. In the present study, structural data for the high-pressure polymorphs were obtained for only a few pressure points, thus we could not properly constrain changes in the equation of state from experiments alone. Instead, we analyzed the DFT results on the end-member composition to estimate the changes in compressibility and volume discontinuities

and compared our results with the calculated results of several important minerals in the transition zone and lower mantle (Figure 4a). The volumes calculated by DFT are usually ~3% smaller than experimental results because of neglecting vibrational contributions (Hu et al., 2016; Qin et al., 2016); however, the relative values give good approximations. The calculated bulk modulus from third-order Birch-Murnaghan equation of state for the $\alpha$-phase was 128(4) GPa, with $K_0' = 4.0(2)$ and $V_0 = 422.1(6)$ Å$^3$. The transformation to $\beta$-diopside increases the bulk modulus to $K_0 = 159(6)$ GPa, $K_0' = 3.6(3)$, and $V_0 = 396.5(7)$ Å$^3$, and results in a 4.3% density increase. The $\gamma$-phase is characterized by $K_0 = 170(5)$ GPa, $K_0' = 3.87(8)$, and $V_0 = 386(1)$ Å$^3$ and is accompanied by 1.5% density increases. The densities of both $\beta$ and $\gamma$-phases lie in the bracket determined by shock experiments (3.6–3.9 g/cm$^3$) (Svendsen & Ahrens, 1983, 1990), it is therefore possible that the phase transformation reported in the shock experiment corresponds to formation of one of the metastable high-pressure phases observed in our study. The temperature in previous shock experiments was estimated to reach ~1,200°C, which indicates that this phase could exist at ~1,200°C and ~90 GPa. The bulk moduli and bulk velocity ($v = \sqrt{K_T/\rho}$) of different phases are also calculated as a function of pressure (Figures 4b and 4c). The new $\beta$ and $\gamma$-diopside are stiffer than $\alpha$-diopside and have higher bulk sound velocity. However, in comparison, bridgmanite (Mg-Pv), Ca-perovskite (Ca-Pv) and akimotoite (Akm) have much higher bulk modulus and bulk sound velocity than the $\alpha$, $\beta$, and $\gamma$-diopside. The $\gamma$-diopside is ~6% and ~11% lighter than $MgSiO_3$ akimotoite (Karki et al., 2000) and $CaSiO_3$+ $MgSiO_3$ perovskite mixture (Caracas et al., 2005; Wentzcovitch et al., 2004), which would promote stagnation of the cold slab in the transition zone or the uppermost part of the lower mantle (Fukao & Obayashi, 2013). In terms of elastic anisotropy, we expect both the $\beta$- and $\gamma$-phases to resemble diopside and akimotoite, which are highly anisotropic (Sang & Bass, 2014), consistent with seismic observation in the cold stagnant slab (Chen & Brudzinski, 2003; Vavryčuk, 2006).

## 4. Conclusions

The fate of clinopyroxenes like diopside in the Earth's mantle is to break down into dense oxides or densify into perovskite phases, with separation of Ca-rich and Ca-poor components. Petrologists previously assumed that this process requires complete breakdown of the crystal structure and involves a fully reconstructive transformation mechanism, with extensive bond breaking and re-formation, and thus requires high temperature to overcome kinetic barriers. The results reported above demonstrate that there exists an alternative path to accomplish the silica densification, which involves a displacive, reversible mechanism and a phase with exotic, penta-coordinated silicon. This general mechanism seems to be accessible to most pyroxenes belonging to the En-Fs-Hd-Di quadrilateral, for both clinopyroxene and orthopyroxene compositions, and it seems to always involve phases with penta-coordinated Si. The presence of $^{V}$Si has consequences for chemical reactivity, elastic and plastic deformation, density of the subducted slab, and its buoyancy relative to the surrounding mantle. In old and cold subducted slabs in the west Pacific region, high-pressure and moderate-temperature conditions along the slab may support such a transformation mechanism and promote metastable existence of $\beta$ and $\gamma$-diopside far outside of their thermodynamic stability fields in the lower mantle.

**Acknowledgments**
The project was supported by the National Science Foundation Division of Earth Sciences Geophysics grant 1344942 to P. D. Development of the ATREX software, used for experimental data analysis was supported by NSF EAR GeoInformatics grant 1440005. Portions of the X-ray diffraction work were conducted using X-ray Atlas instrument at the University of Hawaii, funded by NSF EAR Instrumentation and Facilities grant 1541516. Portions of this work were performed at GeoSoilEnviroCARS (Sector 13), Partnership for Extreme Crystallography program (PX^2), Advanced Photon Source (APS), Argonne National Laboratory. GeoSoilEnviroCARS is supported by the National Science Foundation-Earth Sciences (EAR-1128799) and Department of Energy-Geosciences (DE-FG02-94ER14466). PX^2 program is supported by COMPRES under NSF Cooperative agreement EAR-1661511. Use of the COMPRES-GSECARS gas loading system was supported by COMPRES under NSF cooperative agreement EAR-1661511. Use of the Advanced Photon Source was supported by the U.S. Department of Energy, Office of Science, Office of Basic Energy Sciences, under contract DE-AC02-06CH11357. We would also like to thank Carnegie-DOE Alliance Center for support through Academic Partner subcontract to P. D. and T. S. Duffy at Princeton University for kindly providing the single crystal samples from the Harry Hess collection. B. K. would like to acknowledge computational resources that were made available by the National Science Foundation through XSEDE under grant DMR TG-110093. We would also like to thank the two anonymous reviewers for their insightful advice and Jeroen Ritsema for handling this paper. Additional data are included in the supporting information.

## References

Agrusta, R., van Hunen, J., & Goes, S. (2014). The effect of metastable pyroxene on the slab dynamics. *Geophysical Research Letters*, *41*, 8800–8808. https://doi.org/10.1002/2014GL062159

Akaogi, M., Yano, M., Tejima, Y., Iijima, M., & Kojitani, H. (2004). High-pressure transitions of diopside and wollastonite: Phase equilibria and thermochemistry of $CaMgSi_2O_6$, $CaSiO_3$ and $CaSi_2O_5$-$CaTiSiO_5$ system. *Physics of the Earth and Planetary Interiors*, *143-144*, 145–156.

Angel, R. J., Ross, N. L., Seifert, F., & Fliervoet, T. F. (1996). Structural characterization of pentacoordinate silicon in a calcium silicate. *Nature*, *384*(6608), 441–444.

Asahara, Y., Ohtani, E., Kondo, T., Kubo, T., Miyajima, N., Nagase, T., … Kikegawa, T. (2005). Formation of metastable cubic-perovskite in high-pressure phase transformation of Ca (Mg, Fe, Al) $Si_2O_6$. *American Mineralogist*, *90*(2–3), 457–462.

Badro, J., Teter, D., Downs, R., Gillet, P., Hemley, R., & Barrat, J.-L. (1997). Theoretical study of a five-coordinated silica polymorph. *Physical Review B*, *56*(10), 5797–5806.

Bina, C. R., & Kawakatsu, H. (2010). Buoyancy, bending, and seismic visibility in deep slab stagnation. *Physics of the Earth and Planetary Interiors*, *183*, 330–340.

Blöchl, P. E. (1994). Projector augmented-wave method. *Physical Review B*, *50*(24), 17953.

Canil, D. (1994). Stability of clinopyroxene at pressure-temperature conditions of the transition region. *Physics of the Earth and Planetary Interiors*, *86*(1), 25–34.

Caracas, R., Wentzcovitch, R., Price, G. D., & Brodholt, J. (2005). $CaSiO_3$ perovskite at lower mantle pressures. *Geophysical Research Letters*, *32*, L06306. https://doi.org/10.1029/2004GL022144

Chaplot, S. L., & Choudhury, N. (2001). Molecular dynamics simulations of seismic discontinuities and phase transitions of $MgSiO_3$ from 4 to 6-coordinated silicate via a novel 5-coordinated phase. *American Mineralogist*, *86*(5–6), 752–761.

Chen, W., & Brudzinski, M. R. (2003). Seismic anisotropy in the mantle transition zone beneath Fiji-Tonga. *Geophysical Research Letters*, *30*(13), 1682. https://doi.org/10.1029/2002GL016330

Chopelas, A., & Serghiou, G. (2002). Spectroscopic evidence for pressure-induced phase transitions in diopside. *Physics and Chemistry of Minerals*, *29*, 403–408.
Dera, P., Zhuravlev, K., Prakapenka, V., Rivers, M., Finkelstein, G., Grubor-Urosevic, O., … Downs, R. (2013). High pressure single-crystal micro X-ray diffraction analysis with GSEADARSV software. *High Pressure Research*, *33*(3), 466–484.
Faccenda, M., & Dal Zilio, L. (2017). The role of solid–solid phase transitions in mantle convection. *Lithos*, *268*, 198–224.
Finkelstein, G. J., Dera, P. K., & Duffy, T. S. (2015). Phase transitions in orthopyroxene ($En_{90}$) to 49 GPa from single-crystal X-ray diffraction. *Physics of the Earth and Planetary Interiors*, *244*, 78–86.
Frost, D. J. (2008). The upper mantle and transition zone. *Elements*, *4*(3), 171–176.
Fukao, Y., Obayashi, M., Nakakuki, T., & Deep Slab Project Group (2009). Stagnant slab: A review. *Annual Review of Earth and Planetary Sciences*, *37*, 19–46.
Fukao, Y., & Obayashi, M. (2013). Subducted slabs stagnant above, penetrating through, and trapped below the 660 km discontinuity. *Journal of Geophysical Research: Solid Earth*, *118*, 5920–5938. https://doi.org/10.1002/2013JB010466
Ganguly, J., Freed, A. M., & Saxena, S. K. (2009). Density profiles of oceanic slabs and surrounding mantle: Integrated thermodynamic and thermal modeling, and implications for the fate of slabs at the 660 km discontinuity. *Physics of the Earth and Planetary Interiors*, *172*(3), 257–267.
Hogrefe, A., Rubie, D., Sharp, T., & Seifert, F. (1994). Metastability of enstatite in deep subducting lithosphere. *Nature*, *372*(6504), 351–353.
Holmes, R. R. (1996). Comparison of phosphorus and silicon: Hypervalency, stereochemistry, and reactivity. *Chemical Reviews*, *96*(3), 927–950.
Holzwarth, N., Matthews, G., Dunning, R., Tackett, A., & Zeng, Y. (1997). Comparison of the projector augmented-wave, pseudopotential, and linearized augmented-plane-wave formalisms for density-functional calculations of solids. *Physical Review B*, *55*(4), 2005.
Horiuchi, H. (1987). Perovskite-type $MgSiO_3$-single-crystal X-ray-diffraction study. *American Mineralogist*, *3*, 357–360.
Hu, Q., Shu, J., Cadien, A., Meng, Y., Yang, W., Sheng, H., & Mao, H. (2015). Polymorphic phase transition mechanism of compressed coesite. *Nature Communication*, *6*, 6630.
Hu, Y., Dera, P., & Zhuravlev, K. (2015). Single-crystal diffraction and Raman spectroscopy of hedenbergite up to 33 GPa. *Physics and Chemistry of Minerals*, *42*(7), 595–608.
Hu, Y., Wu, Z., Dera, P. K., & Bina, C. R. (2016). Thermodynamic and elastic properties of pyrope at high pressure and high temperature by first-principles calculations. *Journal of Geophysical Research: Solid Earth*, *121*, 6462–6476. https://doi.org/10.1002/2016JB013026
Irifune, T., Miyashita, M., Inoue, T., Ando, J., Funakoshi, K., & Utsumi, W. (2000). High-pressure phase transformation in $CaMgSi_2O_6$ and implications for origin of ultra-deep diamond inclusions. *Geophysical Research Letters*, *27*, 3541–3544.
Ita, J., & Stixrude, L. (1992). Petrology, elasticity, and composition of the mantle transition zone. *Journal of Geophysical Research*, *97*, 6849–6866.
Karki, B., Duan, W., Da Silva, C., & Wentzcovitch, R. (2000). Ab initio structure of $MgSiO_3$ ilmenite at high pressure. *American Mineralogist*, *85*(2), 317–320.
Kim, Y.-H., Ming, L. C., & Manghnani, M. H. (1994). High-pressure phase transformations in a natural crystalline diopside and a synthetic $CaMgSi_2O_6$ glass. *Physics of the Earth and Planetary Interiors*, *83*(1), 67–79.
King, S., Frost, D., & Rubie, D. (2015). Why cold slabs stagnate in the transition zone. *Geology*, *43*(3), 231–234.
Kirby, S. H., Stein, S., Okal, E. A., & Rubie, D. C. (1996). Metastable mantle phase transformations and deep earthquakes in subducting oceanic lithosphere. *Reviews of Geophysics*, *34*(2), 261–306.
Kresse, G., & Furthmüller, J. (1996a). Efficiency of ab-initio total energy calculations for metals and semiconductors using a plane-wave basis set. *Computational Materials Science*, *6*(1), 15–50.
Kresse, G., & Furthmüller, J. (1996b). Efficient iterative schemes for ab initio total-energy calculations using a plane-wave basis set. *Physical Review B*, *54*(16), 11169.
Liebau, F. (1984). Pentacoordinate silicon intermediate states during silicate condensation and decondensation. Crystallographic support. *Inorganica Chimica Acta*, *89*(1), 1–7.
Liu, L.-G. (1979). The system enstatite-wollastonite at high pressures and temperatures, with emphasis on diopside. *Physics of the Earth and Planetary Interiors*, *19*(3), P15–P18.
Mao, H., Xu, J., & Bell, P. (1986). Calibration of the ruby pressure gauge to 800 kbar under quasi-hydrostatic conditions. *Journal of Geophysical Research: Solid Earth*, *91*(B5), 4673–4676.
Marton, F. C., Bina, C. R., Stein, S., & Rubie, D. C. (1999). Effects of slab mineralogy on subduction rates. *Geophysical Research Letters*, *26*(1), 119–122.
Momma, K., & Izumi, F. (2011). Vesta 3 for three-dimensional visualization of crystal, volumetric and morphology data. *Journal of Applied Crystallography*, *44*(6), 1272–1276.
Morimoto, N. (1988). Nomenclature of pyroxenes. *Mineralogy and Petrology*, *39*(1), 55–76.
Nishi, M., Kato, T., Kubo, T., & Kikegawa, T. (2008). Survival of pyropic garnet in subducting plates. *Physics of the Earth and Planetary Interiors*, *170*(3), 274–280.
Nishi, M., Kubo, T., & Kato, T. (2009). Metastable transformations of eclogite to garnetite in subducting oceanic crust. *Journal of Mineralogical and Petrological Sciences*, *104*(3), 192–198.
Nishi, M., Kubo, T., Kato, T., Tominaga, A., Funakoshi, K.-i., & Higo, Y. (2011). Exsolution kinetics of majoritic garnet from clinopyroxene in subducting oceanic crust. *Physics of the Earth and Planetary Interiors*, *189*(1), 47–55.
Nishi, M., Kubo, T., Ohfuji, H., Kato, T., Nishihara, Y., & Irifune, T. (2013). Slow Si-Al interdiffusion in garnet and stagnation of subducting slabs. *Earth and Planetary Science Letters*, *361*, 44–49.
Oguri, K., Funamori, N., Sakai, F., Kondo, T., Uchida, T., & Yagi, T. (1997). High-pressure and high-temperature phase relations in diopside $CaMgSi_2O_6$. *Physics of the Earth and Planetary Interiors*, *104*, 363–370.
Pakhomova, A., Bykova, E., Bykov, M., Glazyrin, K., Gasharova, B., Liermann, H.-P., … Dubrovinsky, L. (2017). A closer look into close packing: Pentacoordinated silicon in a high-pressure polymorph of danburite. *IUCrJ*, *4*, 671–677.
Pakhomova, A., Ismailova, L., Bykova, E., Bykov, M., Boffa Ballaran, T., & Dubrovinsky, L. (2017). A new high-pressure phase transition in clinoferrosilite: In situ single-crystal X-ray diffraction study. *American Mineralogist*, *102*(3), 666–673.
Perdew, J. P., & Zunger, A. (1981). Self-interaction correction to density-functional approximations for many-electron systems. *Physical Review B*, *23*(10), 5048.
Plonka, A., Dera, P., Irmen, P., Rivers, M., Ehm, L., & Parise, J. (2012). $\beta$-diopside, a new ultrahigh-pressure polymorph of $CaMgSi_2O_6$ with six-coordinated silicon. *Geophysical Research Letters*, *39*, L24307. https://doi.org/10.1029/2012GL054023
Qin, T., Wu, F., Wu, Z., & Huang, F. (2016). First-principles calculations of equilibrium fractionation of O and Si isotopes in quartz, albite, anorthite, and zircon. *Contributions to Mineralogy and Petrology*, *171*(11), 91.

Rasul, G., Prakash, G. S., & Olah, G. A. (2011). Comparative study of the hypercoordinate carbonium ions and their boron analogs: A challenge for spectroscopists. *Chemical Physics Letters*, *517*(1), 1–8.
Ringwood, A. E. (1982). Phase transformations and differentiation in subducted lithosphere: implications for mantle dynamics, basalt petrogenesis, and crustal evolution. *The Journal of Geology*, *90*, 611–643.
Rubie, D. C., & Ross, C. R. (1994). Kinetics of the olivine-spinel transformation in subducting lithosphere: Experimental constraints and implications for deep slab processes. *Physics of the Earth and Planetary Interiors*, *86*(1-3), 223–243.
Sang, L., & Bass, J. D. (2014). Single-crystal elasticity of diopside to 14 GPa by Brillouin scattering. *Physics of the Earth and Planetary Interiors*, *228*, 75–79.
Sanloup, C., Drewitt, J., Konopkova, Z., Dalladay-Simpson, P., Morton, D., Rai, N., … Morgenroth, W. (2013). Structural change in molten basalt at deep mantle conditions. *Nature*, *503*(7474), 104–107.
Schmeling, H., Monz, R., & Rubie, D. C. (1999). The influence of olivine metastability on the dynamics of subduction. *Earth and Planetary Science Letters*, *165*(1), 55–66.
Sheldrick, G. (2008). A short history of shelx. *Acta Crystallographica Section A*, *64*(1), 112–122.
Subramanian, A. (1962). Pyroxenes and garnets from charnockites and associated granulites. *Bulletin of the Geological Society of America*, *Buddington vol.*, 21–36.
Sun, N., Stixrude, L., de Koker, N., & Karki, B. (2011). First principles molecular dynamics simulations of diopside ($CaMgSi_2O_6$) liquid to high pressure. *Geochimica et Cosmochimica Acta*, *75*(13), 3792–3802.
Svendsen, B., & Ahrens, T. J. (1983). Dynamic compression of diopside and salite to 200 GPa. *Geophysical Research Letters*, *10*(7), 501–504.
Svendsen, B., & Ahrens, T. J. (1990). Shock-induced temperatures of $CaMgSi_2O_6$. *Journal of Geophysical Research*, *95*(B5), 6943–6953.
Tandura, S. N., Voronkov, M. G., & Alekseev, N. V. (1986). Molecular and electronic structure of penta-and hexacoordinate silicon compounds, *Structural Chemistry of Boron and Silicon* (pp. 99–189). Berlin: Springer.
Tetzlaff, M., & Schmeling, H. (2000). The influence of olivine metastability on deep subduction of oceanic lithosphere. *Physics of the Earth and Planetary Interiors*, *120*(1), 29–38.
Thompson, R., & Downs, R. (2008). The crystal structure of diopside at pressure to 10 GPa. *American Mineralogist*, *93*, 177–186.
Van Mierlo, W., Langenhorst, F., Frost, D., & Rubie, D. (2013). Stagnation of subducting slabs in the transition zone due to slow diffusion in majoritic garnet. *Nature Geoscience*, *6*(5), 400–403.
Vavryčuk, V. (2006). Spatially dependent seismic anisotropy in the Tonga subduction zone: A possible contributor to the complexity of deep earthquakes. *Physics of the Earth and Planetary Interiors*, *155*(1), 63–72.
Walker, A. M. (2012). The effect of pressure on the elastic properties and seismic anisotropy of diopside and jadeite from atomic scale simulation. *Physics of the Earth and Planetary Interiors*, *192*, 81–89.
Walker, A. M., Tyer, R. P., Bruin, R. P., & Dove, M. T. (2008). The compressibility and high pressure structure of diopside from first principles simulation. *Physics and Chemistry of Minerals*, *35*(7), 359–366.
Wentzcovitch, R., Karki, B., Cococcioni, M., & De Gironcoli, S. (2004). Thermoelastic properties of $MgSiO_3$-Perovskite: Insights on the nature of the Earth's lower mantle. *Physical Review Letters*, *92*(1), 018501.
White, E. T., Tang, J., & Oka, T. (1999). $Ch^{5+}$: The infrared spectrum observed. *Science*, *284*(5411), 135–137.
Xu, J., Zhang, D., Fan, D., Downs, R. T., Hu, Y., & Dera, P. K. (2017). Isosymmetric pressure-induced bonding increase changes compression behavior of clinopyroxenes across jadeite-aegirine solid solution in subduction zones. *Journal of Geophysical Research: Solid Earth*, *122*, 142–157. https://doi.org/10.1002/2016JB01350
Yuan, F., & Huang, L. (2014). Brittle to ductile transition in densified silica glass. *Scientific Reports*, *4*, 5035.
Zhang, D., Hu, Y., & Dera, P. K. (2016). Compressional behavior of omphacite to 47 GPa. *Physics and Chemistry of Minerals*, *43*(10), 707–715.
Zhang, J., Green, H. W., & Bozhilov, K. N. (2006). Rheology of omphacite at high temperature and pressure and significance of its lattice preferred orientations. *Earth and Planetary Science Letters*, *246*(3), 432–443.